Elsevier Editorial System(tm) for Composites Part B

Manuscript Draft

Manuscript Number: JCOMB-D-16-00611

Title: Novel "load adaptive algorithm based" procedure for 3D printing of cancellous bone-inspired structures

Article Type: SI: COMPOSITE LATTICE

Keywords: A. Fibres; B. Directional orientation; C. Finite element analysis (FEA); D. Mechanical testing; 3-Dimensional printing.

Corresponding Author: Dr. Francesco Naddeo, Ph.D.

Corresponding Author's Institution: University of Salerno

First Author: Francesco Naddeo, Ph.D.

Order of Authors: Francesco Naddeo, Ph.D.; Nicola Cappetti, Master Degree; Alessandro Naddeo, Master Degree

Abstract: This work shows the practical application and the experimental validation of a procedure based on an original algorithm, running in a finite element environment, able to operate inside any three-dimensional solid by replacing the continuous mass with an appropriate cancellous bone-inspired space-frame sharing, with the concrete model, the border and organized for having the fibres oriented according to the boundary conditions. The purpose is to reach the maximum mechanical efficiency realizing a load adaptive space-frame optimized in terms of weight. Young's moduli of a cubic virtual specimen were numerically estimated. Fifteen specimens were printed by a 3D printer using an appropriate titanium alloy. Numerical results were compared with experimental ones obtained by tensile tests. The simulation results confirmed the validity of the FEM "beam element - based" space frame.

Suggested Reviewers: Luca Di Angelo Ph.D.
Associate Professor, Department of Industrial and Information Engineering and Economics, University of L'Aquila
luca.diangelo@univaq.it
Luca Di Angelo has developed strong skills in the computational graphic design and in writing algorithms managing parametric variational CAD models.

Ernesto Reverchon
Full Professor, Department of Industrial Engineering, University of Salerno, Via Giovanni Paolo II, 132, 84084 Fisciano, SA, Italy
ereverchon@unisa.it
Ernesto Reverchon has developed strong skills in design and production of porous structures showing at the same time different levels of porosity to be used in the contest of computer aided tissue engineering.

Giovanni Francesco Solitro Ph.D.
Research Associate, Department of Orthopaedics, University of Illinois at Chicago, 835 South Wolcott Avenue. Chicago, United States of America
solitrogf@hotmail.com

Giovanni Francesco Solitro has developed strong skills in the Biomechanics especially in the mechanical characterization of the bone tissue and in the parametric variational CAD modeling.

Opposed Reviewers:

Dear Editor

The paper entitled "*Novel "load adaptive algorithm based" procedure for 3D printing of cancellous bone-inspired structures*" by Francesco Naddeo, Nicola Cappetti and Alessandro Naddeo is an original article. The manuscript, including related data, figures and tables, has not been previously published and is not under consideration elsewhere.

This work shows the practical application and the experimental validation of a procedure based on an original algorithm (filed patent) that runs in a finite element environment; it operates inside a three-dimensional virtual solid of any shape, withstanding any kind of boundary conditions for both imposed displacements and loads (in the field of the static structures) replacing the continuous mass of the solid with an appropriate space-frame structure, having cylindrical beams directed according to the internal stresses induced by the boundary conditions, the new structure and the old one sharing the border.

Other works in the contest of computational aided tissue engineering (CATE) focused on the realization of porous models (to be printed) that do not care about the real boundary conditions and whose geometric parameters are difficult to manage.

In this case the user can manage several input parameters like average minimum distance between convergence nodes, target porosity, target average number of beams converging in each node and beams' mechanical properties. A cubic representative volume element was appropriately designed and sized to conduct sensitivity analyzes to show the effect of changes in these parameters on the mechanical performances of the new porous material. The finite element results were compared with experimental results obtained by tensile tests conducted on a metallic 3D printed cubic specimen. The simulation results, in terms of Young's modulus, confirmed the validity of the beam element - based space frame that could be applied to different solid shapes and materials.

Possible applications will be the production of those porous materials for which it is required a set value of porosity, a set external shape, a low weight and heterogeneity of

the mechanical properties at the micro and macro levels as for example in the field of the CATE for production of scaffolds (bone-like structured foams) and in the field of ergonomics for production of highly structured foams.

I will be glad if you want to consider my paper for publication in "*COMPOSITES PART B: ENGINEERING: JCOMB" - SPECIAL ISSUE ON "COMPOSITE LATTICE MATERIALS AND STRUCTURES".*

Thank you for your consideration,

Sincerely

Francesco Naddeo

Novel "load adaptive algorithm based" procedure for 3D printing of cancellous bone-inspired structures

Francesco Naddeo[a], Nicola Cappetti[a], Alessandro Naddeo[a]

[a] Department of Industrial Engineering, University of Salerno, Via Giovanni Paolo II, 132, 84084 Fisciano (SA) Italy.

frnaddeo@unisa.it, ncappetti@unisa.it, anaddeo@unisa.it

Corresponding author: Francesco Naddeo; frnaddeo@unisa.it

Abstract

This work shows the practical application and the experimental validation of a procedure based on an original algorithm, running in a finite element environment, able to operate inside any three-dimensional solid by replacing the continuous mass with an appropriate cancellous bone-inspired space-frame sharing, with the concrete model, the border and organized for having the fibres oriented according to the boundary conditions. The purpose is to reach the maximum mechanical efficiency realizing a load adaptive space-frame optimized in terms of weight. Young's moduli of a cubic virtual specimen were numerically estimated. Fifteen specimens were printed by a 3D printer using an appropriate titanium alloy. Numerical results were compared with experimental ones obtained by tensile tests. The simulation results confirmed the validity of the FEM "beam element – based" space frame.

Keywords

A. Fibres; B. Directional orientation; C. Finite element analysis (FEA); D. Mechanical testing; 3-Dimensional printing.

1. Introduction

Since 2000 [1] researchers have developed, improved, and applied already existing finite element-based topology optimization methods [2]. The target was to create optimized structures for loads, with special attention given to the amount of material used as a means to reduce costs and lighten the structure. The most important types of topology optimization methods are: density-based methods, which include the popular Solid Isotropic Material with Penalization (SIMP) technique, hard-kill methods, including Evolutionary Structural Optimization (ESO), boundary variation methods and biologically inspired methods. Biologically inspired methods

are based on the fact that living beings have developed biological tissues characterized by such optimized structures. In the contest of bone tissue, Wolff [3], who described the trajectorial theory of trabecular orientation, suggests that bone obtained maximum mechanical efficiency with minimum mass and that trabecular bone architecture undergoes adaptive changes. Several mathematical models have been proposed for bone remodelling and various criticisms have been made on Wolff's law about the one-to-one correspondence between the stress trajectories of continuous bodies and the discontinuous structure of the bone [4]. The proposed models usually assumed bone tissue final configuration as a function of boundary conditions and bone to be a continuous, linearly elastic material. Anisotropic continuum-based models were used by Fernandes et al [5], Garcia et al [6] and Jacobs et al [7], while orthotropic continuum-based models were used by Cowin [8] and Huiskes and Hollister [9]. Tsubota et al [10] used large-scale voxel finite element models (FEMs) for simulating the trabecular bone remodelling. Luo and An [11] and Boyle and Kim [12] proposed optimization techniques, while Hambli et al [13] introduced a coupled finite element and neural network computation method. Currently, finite element analysis is increasingly used as a means to design new structures generally used for composite materials or porous materials. In this case, FEM results become input parameters managed by highly complex algorithms that, by means of looping procedures, are able to optimize virtual structures respect to a particular mechanical aspect.

The aim of this work was to create a highly structured 3D printed porous material biologically inspired by means of an original algorithm which, in the same manner of biological tissues and, in this paper's case, of cancellous bone (on the base of Wolff's law), is able to adapt the internal structure to external loading conditions, showing, at the same time, a lightweight structure with the possibility to parameterize the homogenized mechanical properties by simply varying the sensitive parameters that describe the geometry of the structure. In many fields of research on the highly structured porous materials, the production is often bound to the use of particular materials, to respect a particular external geometrical shape and a particular porosity, i.e., a particular amount of material. In the area of Computer Aided Tissue Engineering (CATE) for the production of scaffolds, materials used for bone regeneration have to mimic the behaviour and the architecture of natural biological tissue; this one is naturally optimized to withstand the loads

to which it is subjected during its life cycle. Furthermore, in the design of such structures you must take into account the boundary conditions characterizing the period they will spend in bioreactors in which they will be subjected to different types of mechanical stimuli both static and dynamic.

The proposed algorithm [14], runs in a finite element environment; it operates inside a three-dimensional virtual solid of any shape, withstanding any kind of boundary conditions for both imposed displacements and loads (in the contest of the static structures) replacing the continuous mass of the solid with an appropriate space-frame structure, having cylindrical beams directed according to the internal stresses induced by the boundary conditions, the new structure and the old one sharing the border. A cubic representative volume element (RVE) was appropriately designed and sized to conduct sensitivity analyzes to show the effect of changes in these parameters on the mechanical performances of the new porous material. The finite element results were compared with experimental results obtained by tensile tests conducted on a metallic 3D printed cubic specimen. The simulation results, in terms of Young's modulus, confirmed the validity of the beam element - based space frame that could be applied to different solid shapes and materials.

2. Materials and Methods

The algorithm realized for this work, runs in Ansys FEM environment and is able to build, inside a virtual solid of any geometric shape, a virtual beam network (beams of any length, of any type of section and aspect ratio) with beam elements connected each other at the end points with internal fixed joints. The network, at the beginning, shows randomly oriented beams and shares with the solid the border. The algorithm remodels the beam network obtaining a structure having the beams oriented mostly along the principal stress directions recorded in the continuous mass whose convergence nodes have a desired average number of connections. After appropriate sizing of the beams, the algorithm, while ensuring the structural continuity of the beam network, allowed for the creation of a new structure able to efficiently withstand the same boundary conditions with a considerable lightening of the structure, and, consequently, a remarkable reduction in materials used.

2.1 Description of the algorithm

The algorithm is written in a single source code using ANSYS Parametric Design Language (APDL); below is the algorithm pseudocode divided into macro steps (Figure 1):

1. It takes in input the three-dimensional CAD (Computer Aided Design) geometry of the solid;
2. It creates a random distribution of keypoints (keypoints' cloud) inside the external surface of the solid;
3. It defines a spherical space of selection (SSS) for each generated keypoint, in order to intercept a specified number of keypoints [15] and generates line segments joining the initial keypoint (centred in its SSS), with each keypoint belonging to its SSS;
4. It conveniently eliminates both overlaps and intersections among line segments;
5. It creates the mesh of each line segment by means of beam elements [15, 16]; the obtained space frame shows an isotropic mechanical behaviour;
6. After applying to the FEM model linear material properties, characterizing the real material behaviour, it applies boundary conditions simulating current conditions;
7. It calculates the elastic solution due to the boundary conditions defined in step 6;
8. In post-processing, it build an array where all the identification numbers of the created beams are sorted in an ascending order according to an appropriate criterion based on the magnitude of the stresses to which each element is subjected during the FEM virtual test.
9. It activates an iterative routine that, according to the array created in step 8, eliminates the beams starting from the first component of the array. The iteration stops at a specified number of beams such that the number of connections for each convergence node is equal to the predefined average number of beams (ANB) converging on each node; simultaneously it activates an *ad hoc* routine able to guarantee structural continuity;
10. It activates a routine that eliminates the so-called "dead ends"; i.e., the branches of the structure made of beams that, having a single point of connection with the rest of the structure, will not work [17];

11. It resizes the cross section of the beam according to the desired porosity (defined as the fraction of the volume of voids over the total volume of the inputted solid) or to the wanted mechanical stiffness.
12. It generates in CAD environment the solid model;
13. It generates the file .stl for the following rapid prototyping phase in order to obtain the physical model.

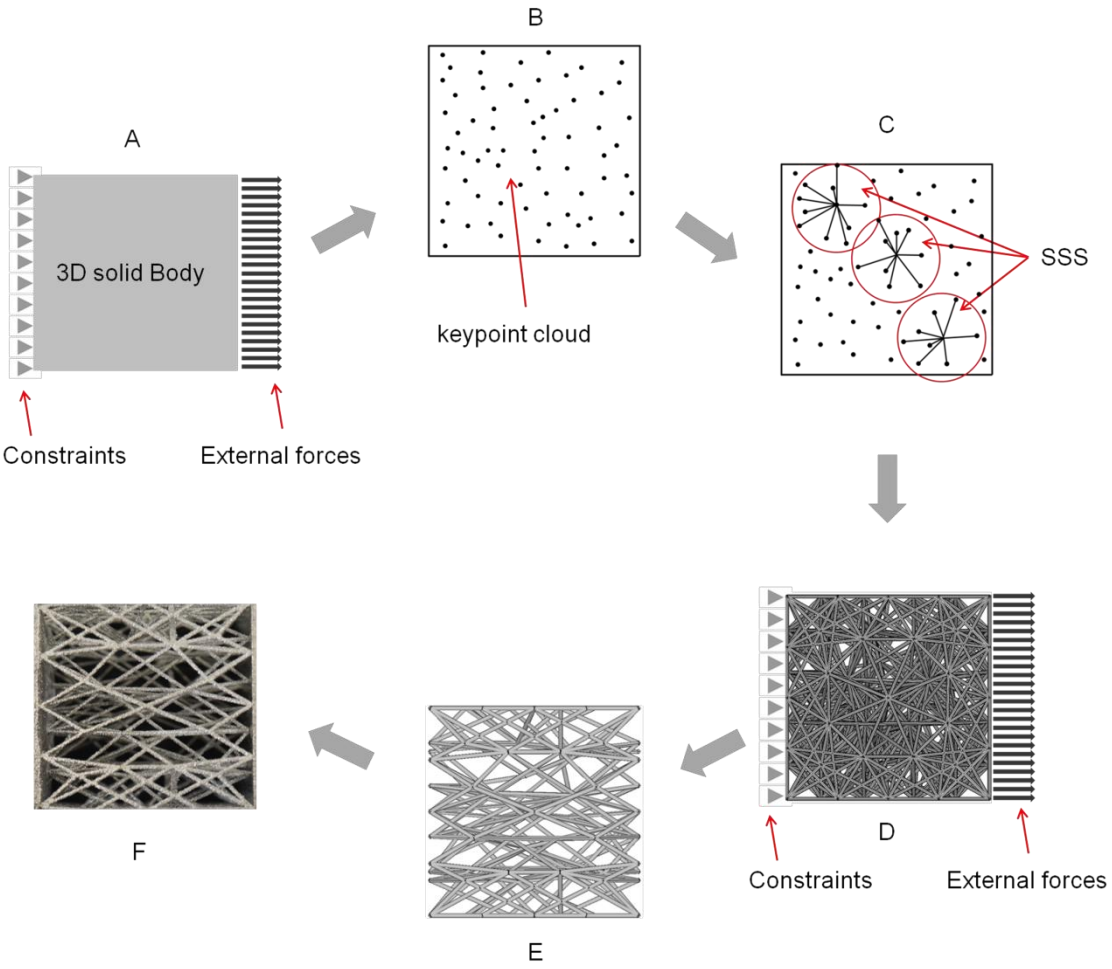

Figure 1. Algorithm flow chart showing the fundamental steps used for elaborating a cubic solid mass withstanding generic boundary conditions: A) step 1; B) step 2; C) steps 3 and 4; D) steps 5 - 8 ; E) steps 9 - 13; F) 3D printed metal specimen.

In the past, researchers [18] created three-dimensional beam-based structures interpolating only the principal stress directions so that they did not select other elements that, being oriented not along isostatic lines may constitute real bracings and improve structural performance. In this

work, the initial randomly oriented beam network (see steps 5), allows for the most advantageous directions to be chosen to minimize the amount of material used, by eliminating selectively the less loaded beams until reaching a predefined number of converging beams for each convergence node.

2.2 Input parameters

The user, by means of the algorithm, can manage the following input geometric parameters:

- Average minimum distance between convergence nodes (*dist*) defined as a linear function of a characteristic size of the inputted solid;
- Target porosity;
- Target ANB;
- Radius of the SSS, being a linear function of the previously defined "*dist*", that is chosen due to its appropriate ANB;
- Mechanical properties.

2.3 FEM element type

In this work, we have implemented quadratic three-node straight beam elements in 3-D showing circular cross section, which are suitable for analyzing slender to moderately stubby/thick beam structures. It takes into account both torsion-related shear stresses and flexure-related transverse-shear stresses (which henceforth will be generically referred to as "shear stresses (τ)"), as the focus will be on their absolute maximum value and not on their causes. Six degrees of freedom occurred at each node for translations and rotations in directions *X*, *Y* and *Z*.

2.4 FEM mechanical properties

At the beginning, we have realized a sensitivity analysis campaign on input parameters choosing an appropriate cubic RVE; the aims were: 1) the evaluation of the effects of changes in sensitive input parameters, specified in section 2.2, on the mechanical performance of the new material inside the values for which a linear elastic behaviour is shown.; 2) the sizing of the RVE.

For ease of discussion and without any loss of generality, for the mechanical characterization of the beams, the elastic modulus was set to E = 1 Pa while the Poisson's ratio was set to v = 0.3.

Later in the discussion, the chosen morphometric input data and the material properties of the material selected for 3D printing and that have been introduced in the algorithm, will be reported.

2.5 RVE description and boundary conditions

Cubic-shaped RVE (with a unitary volume for ease of discussion and without any loss of generality) was chosen to evaluate the mechanical performance of the algorithm and evaluate the material symmetry imparted by it, on the basis of the boundary conditions; cubic-shaped RVE also allows an easy boundary conditioning.

The target of this work was to optimize the structure of the chosen RVE orienting the beams according to the internal loads induced by the boundary conditions. When a space frame structure exhibits a preferential orientation of the beams along a particular direction (that we can find in cancellous trabecular bone), the porous material behaves like an orthotropic material, and sometimes, more specifically, a transverse isotropic material. In this study, the RVE was subjected to a virtual tensile test along the *X* axis parallel to one of the edges of the cubic RVE to allow the algorithm to properly orient the beams along this axis.

2.5.1 Periodic boundary conditions

All the simulations realized to create and size the FEM model were carried out by applying PBC to the RVE by allowing calculating more accurately the homogenized elastic constants of the RVE [19, 20]. For the specific study of this cubic RVE, an *ad hoc* written FEM routine was used. It can automatically create an identical surface distribution of nodes on the opposite sides [21]. Further, on the basis of their location, these nodes are opportunely selected since the conditions on the displacements, in this case, have to couple the displacements at each point located on opposite sides of the cubic RVE. These conditions can be expressed in the following synthetic matrix the form:

$$u_2 - u_1 = \varepsilon(X_2 - X_1) \quad (1)$$

With ε, being the *strain tensor*, X_i (i = 1, 2) being the position vector of the points belonging to opposite sides of the RVE, and u_i being the relative displacement.

2.5.2 Homogenized modules

The routine described in 2.5.1 for each simulation can automatically perform three virtual static tensile tests and three static shear tests (with imposed average strains) in order to have an exhaustive representation of the mechanical behaviour of the structure. Imposing the overall strain to the RVE: $\langle\varepsilon\rangle = [0 \dots \langle\varepsilon_i\rangle \dots 0]$, and assuming elastic behaviour and small strains of the material, for each i-th imposed strain, the routine allows for calculating all the components of the corresponding i-th column of the stiffness matrix using the following formulation (elastic overall constitutive law):

$$\overline{C_{hi}} = \frac{\langle\sigma_h\rangle}{\langle\varepsilon_i\rangle} \; \forall \; h, \; i = 1,\dots,6 \qquad (2)$$

with $\langle\sigma_h\rangle$ being the stress component calculated in the FEM post-processing environment, using the following relation:

$$\langle\sigma_h\rangle = \frac{\sum_{elem} \sigma_{h_{elem}} vol_{elem}}{vol_{RVE}} \qquad (3)$$

$\sigma_{h_{elem}}$ being the *h-th* stress component of the single FEM element, due to the *i-th* imposed strain, vol_{elem} being the element volume, and vol_{RVE} the volume of the RVE. In this way, the routine can calculate all the components of the stiffness matrix with Eq. 2 by means of a single FEM run, characterized by six sequential imposed strains. Finally, the routine automatically provides the stiffness and compliance matrices of the examined cubic RVE in output.

2.5.3 RVE sizing

As reported previously, the main algorithm, in step 5 (see section 2.1), creates a beam network that tends to show isotropic material behaviour (see Figure 2). In terms of statistics, the increasing of the RVE size (i.e., increasing the number of beams) causes an increase in the material's isotropic degree. For this reason, intrinsic statistical characteristics were taken into consideration when choosing the RVE size in order to obtain an acceptable starting isotropic degree [20]. An original isotropic criterion [21, 22] to optimize the size of the cubic RVE was implemented. It is based on the minimization of the following function:

$$|\Delta|^2 = \sum_{i,j=1}^{6} \left(C_{i,j} - C_{i,j}^{I}(\lambda, G)\right)^2 \qquad (4)$$

with $C_{i,j}$ being the i, j-th component of the stiffness matrix, calculated from the FEM results; $C_{i,j}^{I}$ being the i, j-th component of the unknown isotropic stiffness matrix; and λ and G representing the independent parameters defining the isotropic stiffness matrix (Lamè

constants). The minimization of Eq. 4 led to the determination of λ and G, i.e., the parameters defining the behaviour of the isotropic material closer to the behaviour of the material simulated by the FEM calculation. Consequently, an *ad hoc* written routine calculated the parameter δ, defined as the ratio of the norm of the "difference tensor" $\Delta = C - C^I$ to the norm of the tensor C^I. The parameter δ provided information about the isotropic degree of the cubic RVE, which was directly related to the previously defined parameter "*dist*" of the RVE.

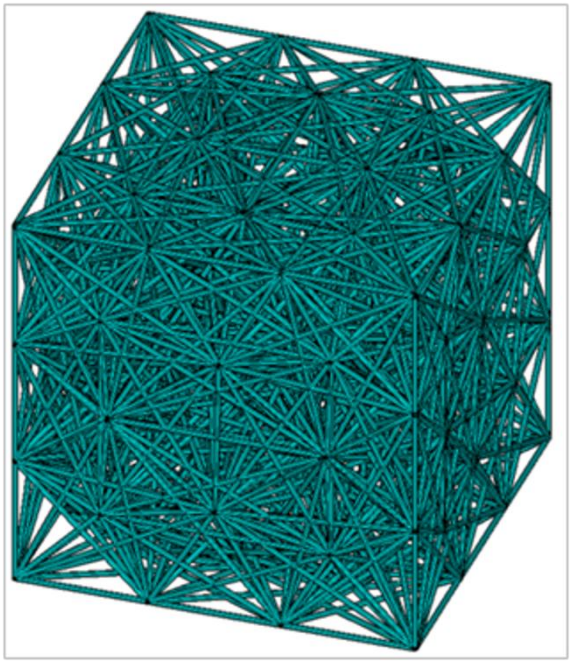

Figure 2. Example of an initial isotropic cubic RVE. For graphical purposes, fewer mesh wires than those used in the calculation are represented.

The isotropic criterion showed that the value of the parameter δ tended towards a small constant value for $dist = \frac{Lrve}{10}$, with $Lrve$ being the edge length of the cubic RVE. In this way, the RVE size was not too large from a computational point of view, but sufficiently large to make the beams substantially oriented in a random way. This structure gave to the RVE a sufficiently isotropic mechanical behaviour prior the application of the boundary conditions designed to orient the beams (see section 2.1, steps 6).

2.6 Convergence analysis of the FEM results

For each beam, with the increasing of the number of elements, we do not have an appreciable variation in the FEM results in terms of homogenized Young's moduli of the RVE. For this reason, each beam was modelled by means of a single beam element [16, 23, 24].

2.7 Beam sorting criteria

In the post-processing environment (see section 2.1, step 8), the algorithm sorts, in an array, all the identification numbers of the created beams in an ascending order according to an appropriate criterion based on the magnitude of the stresses to which each element is subjected during the virtual test. The choice of the criterion should be conducted considering the real behaviour of the simulated material (material ductility and brittleness) and the boundary conditions. In the present study, three different output entities were considered for each beam element:

- The quantity of elastic strain energy stored during the calculation,

  $$\emptyset = \int C_{ijhk}\varepsilon_{ij}d\varepsilon_{hk} \quad (5)$$

  with C_{ijhk} being the generic component of the elastic tensor of fourth order, and ε_{ij} and ε_{hk} the generic strain components;
- Maximum equivalent von Mises stress ($\sigma_{eq,\ Max\ (von\ Mises)}$);
- Maximum principal stress absolute value ($\sigma_{principal,\ Max}$);

The criteria based on the maximum equivalent von Mises stress and on the maximum principal stress absolute value derive from considerations about the behaviour of the studied material. In the first criterion, a selection based on the amount of distortion energy stored by the beams during simulated tension/compression test (von Mises failure criterion for ductile material) is preferred. The second criterion, conversely, only considers the effect of the normal stresses stored in the beams (Coulomb and Mohr failure criteria for brittle materials). To achieve this, the main algorithm is equipped with specific routines designed to calculate/retrieve and sort the above variables for each element in the post-processing environment (see section 2.1, steps 8 and 9).

2.8. Sensitivity analysis campaign

A sensitivity analysis campaign on input geometric parameters was realized on an appropriate cubic RVE, after the orientation of the beams, with the aim to evaluate the effects of changes in

SSS and ANB, on the mechanical performance of the new material under linear elastic behaviour hypothesis. We have used a simple “one factor at a time” approach, estimating the influence of these geometric parameters on the mechanical behaviour of the RVE by independently varying them over an appropriate range. However, this approach is unable to reveal clearly possible interactions among parameters [25] but it gives us information about the potentiality in managing of such an algorithm in order to optimize the results.

2.8.1 Variation of the parameter SSS

The SSS size must ensure an initial ANB as to have an enough large number of orientations to be selected. An excessive large SSS size, however, could determine intersections among beams with related computational problems, difficulties to model in CAD environment, with subsequent inability to create the .stl file for 3D printing. For this reason three values of SSS radius (1.5 x *dist*, 1.75 x *dist* and 2 x *dist*) were considered, the other input parameters being constant. The authors have judged the value of SSS radius equal to 1.75 x *dist* a fair compromise between fairly high value of the Young’s moduli (E_x, E_y and E_z, being X, Y and Z the three directions parallel to the three mutually perpendicular edges of the RVE) and the risk of possible intersections among beams (if the beams remain, on average, of the same length, the probability that they intersect each other is greatly reduced). Furthermore, in this way there is a better accuracy in modelling the boundary of the solid when it presents curvatures with a radius of the same order of magnitude as the average minimum distance between the convergence nodes.

2.8.2 Variation of the parameter ANB

Subsequently, once set the SSS size, ANB was varied from a minimum of 4, to a maximum of 20. It was found that the homogenized Young’s modulus of the cubic RVE, in the loading direction (E_x), tends to decrease with increasing of ANB, while the other two Young's moduli (E_y and E_z) tend to increase, thus tending to the same value for ANB greater than 12. Thinking of a future production of bone scaffolds that have to mimic, among other things, also the geometric distribution of the trabeculae, ANB equal to 6 was chosen also taking into account the average number of converging trabecula characterizing the transversely isotropic cancellous bone [16].

3. Three dimensional printing and mechanical tests

One virtual model, characterized by the morphometric input data collected in the Table 1, was created using the algorithm described in this work that oriented the beams along the *X* axis. The aim was to print three-dimensional specimens to be tested in order to study the experimental/numerical correlation. The target of this phase of the study was to validate the FEM model characterized by a one-dimensional element (beams) based network. In this case, for ease of discussion and without any loss of generality, the parameters "*Lrve*" (length of the cubic RVE), "*dist*" and the porosity have been sized taking into account the type of technology adopted for 3D printing, its accuracy and the available testing machine (load cell of the testing machines). The algorithm has provided, in output, an .iges file containing a set of solids representing the beams (cylinders generated by the algorithm) and the convergence nodes (spheres whose radius is equal to the cylinders' radius).

Table 1 Morphometric input parameters characterizing the cubic RVE to be printed.

	RVE
Lrve	4cm
dist	Lrve/4
SSS radius	*dist* x 1.75
Porosity	0.96
ANB	6

This file has been treated with a special routine in CAD simulation environment to fuse the various solids together and create the .stl file to be supplied to the 3D printer. For the realization of the specimens we have used an ARCAM Q20 3D printer (Electron Beam additive Manufacturing). To ensure a good grip, the specimens were equipped with rigid bases having two suitably filleted cylinders (see Figure 3).

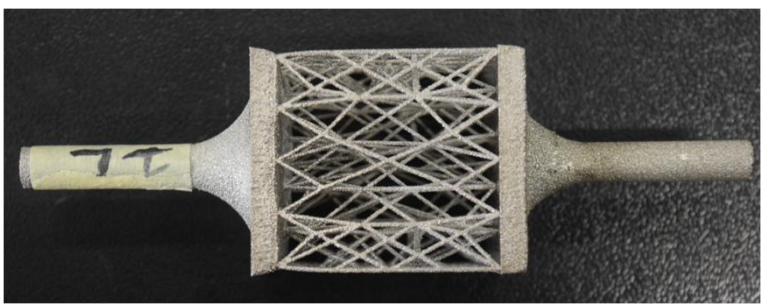

Figure 3. 3D printed titanium alloy specimen.

Tensile mechanical properties of the printed material were measured using an electromechanical testing machine MTS Insight 30 (see Table 2 and Figure 4).

Table 2 Testing machines characteristics

force capacity:	30kN
load cell accuracy:	class 0.5
position resolution:	0.001 mm
position accuracy:	0.01 mm
axial extensometers	MTS 634.12F-24
gage length	25 mm
accuracy class	0.5 mm

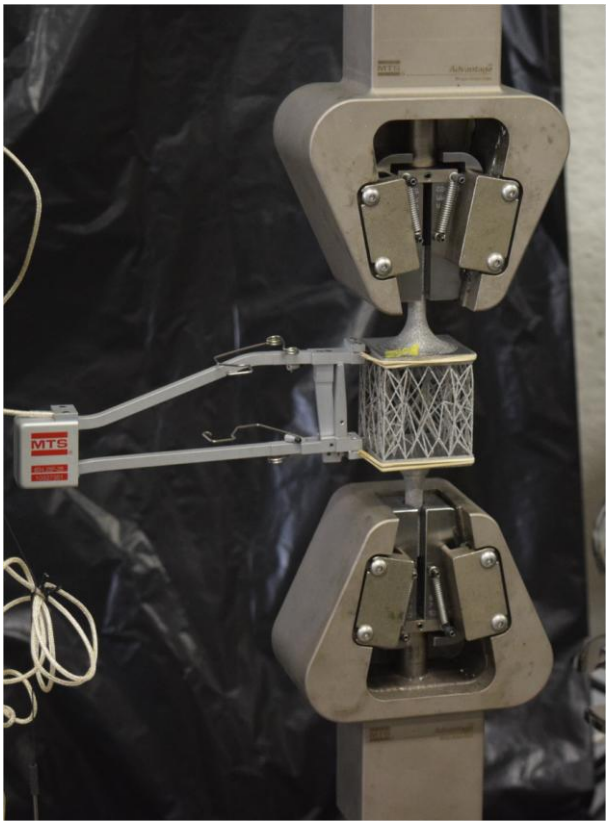

Figure 4. Tensile test on the cubic specimen.

The cubic specimens were tested at a cross-head speed of 2mm/min along *X*, *Y* and *Z* directions. The homogenized experimental Young's modulus was defined as the initial linear portion of the stress–strain curve. Five specimens were tested for each tensile direction.

4. Experiments

The algorithm was optimized to process the cubic RVE described in the section 2.5 and characterized by the parameters listed in the Table 1.

The boundary conditions (see section 2.1, steps 6 and 7) used to select the more loaded beams (oriented along the *X* axis) consisted of an overall deformation $\langle\varepsilon\rangle = [\langle\varepsilon_x\rangle \dots 0]$, with $\langle\varepsilon_x\rangle$ being the strain component along the *X* axis set to 10^{-4} for the sake of simplicity.

The algorithm once introduced the experimental mechanical properties and calculated the elastic solution (see section 2.1, steps 7), selected the beams that were directed according to the internal stress by deleting the least stressed beams while maintaining structural continuity (see section 2.1, steps 8 - 10).

Subsequently, after re-applying the PBC, assuming small strains and the elastic behaviour of the material, the routine described in 2.5.1, with a single FEM run characterized by six sequential imposed deformations (three tensile tests and three shear tests respectively in the three directions defined by the mutually perpendicular edges of the RVE), was able to calculate all the components of the stiffness matrix characterizing the new RVE structure.

In this way, it was possible to highlight the material symmetry assumed by the RVE. In the present case, the matrix displays an orthotropic behaviour that tends to a transversely isotropic behaviour with an isotropy axis coinciding with the X axis (see Table 3).

It is possible to find this type of material symmetry in the bone tissue when the trabecular system is oriented along one direction (e.g. the head of the femur) as supported by the literature [8, 9, 16].

Table 3 Cubic RVE stiffness matrix: the values were rounded to the first decimal place to better show the tendency to a transversely isotropic behaviour.

K_{11} = 24.7	K_{12} = 1.7	K_{13} = 1.8	K_{14} = 0.0	K_{15} = 0.0	K_{16} = 0.0
K_{21} = 1.7	K_{22} = 0.6	K_{23} = 0.1	K_{24} = 0.0	K_{25} = 0.0	K_{26} = 0.0

$K_{31} = 1.8$	$K_{32} = 0.1$	$K_{33} = 0.6$	$K_{34} = 0.0$	$K_{35} = 0.0$	$K_{36} = 0.0$
$K_{41} = 0.0$	$K_{42} = 0.0$	$K_{43} = 0.0$	$K_{44} = 0.1$	$K_{45} = 0.0$	$K_{46} = 0.0$
$K_{51} = 0.0$	$K_{52} = 0.0$	$K_{53} = 0.0$	$K_{54} = 0.0$	$K_{55} = 1.9$	$K_{56} = 0.0$
$K_{61} = 0.0$	$K_{62} = 0.0$	$K_{63} = 0.0$	$K_{64} = 0.0$	$K_{65} = 0.0$	$K_{66} = 2.0$

At the end of the routine that gives the orientation to the beams (see section 2.1, steps 9 and 10), the algorithm, on the basis of the pseudocode listed in Section 2.1, resized the beams according to the target porosity, varying the radius of the circular cross section of the beams. Finally, (see section 2.1, steps 13 and 14) the physical models characterized by morphometric parameters listed in table 1 were realized by means of rapid prototyping technique with the purpose of testing them through the tensile test; the three homogenized Young's moduli have been experimentally evaluated in the three mutually perpendicular directions *X*, *Y* and *Z* of the cubic specimen.

Once built the virtual RVEs described in section 3, boundary conditions, approximating the tensile tests, have been applied in Ansys environment, assuming absence of sliding of the zones in contact with the rigid bases characterizing the metal specimen. Then the three homogenized Young's moduli have been numerically evaluated in the three directions *X*, *Y* and *Z* of the cubic RVE.

Figure 5 shows the effect of the algorithm elaboration on the cubic RVE (a and b) and the 3D printed titanium alloy specimen (c).

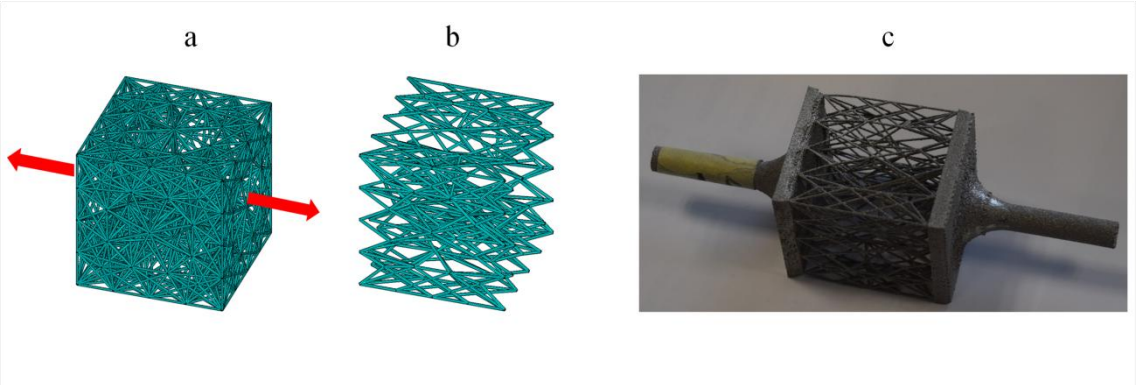

Figure 5. Effect of the algorithm elaboration on the cubic RVE: a) isotropic cubic space frame showing the direction of the imposed displacements (*X* axis); b) cubic space frame showing resized beams oriented along the *X* axis; c) 3D printed titanium alloy specimen.

5. Results

5.1 Beam sorting criteria results

The choice of beam sorting criteria was based on a comparison of the FEM simulation results of the final cubic RVE showing the beams oriented along the *X* axis. For the sake of simplicity, an input Young's modulus for beams equal to $E_i = 1Pa$ and with an overall deformation $\langle \varepsilon_x \rangle = 10^{-4}$ were introduced as input parameters. The results used for comparison were maximum values (*Maxv*) recorded in the whole RVE for von Mises equivalent stress, principal stress (absolute value), and shear stress (absolute value). To understand the average behaviour of the RVE structure and to avoid the possibility that abnormal maximum values could affect the evaluation, it was also considered the arithmetic mean value (*Amv*) of the maximum values recorded in each beam of the same items that was calculated by means of the following formula:

$$Amv = \frac{1}{n}\sum_{i=1}^{n} X_{Max,i} \quad (6)$$

with *n* being the number of beams and $X_{Max,i}$ representing, alternately, the maximum values of von Mises equivalent stress, principal stress (absolute value) and shear stress (absolute value) in the i-th beam.

Finally, a comparison was also made between the homogenized Young's moduli of the RVE, calculated in the preferred direction of the beams (*X*-axis) using the three different criteria. Histograms in Figure 6 show the used criteria and the comparison among them: title, if any, represents the type of result; the criteria are reported on the abscissa axis; the results, to be compared, are reported on legends.

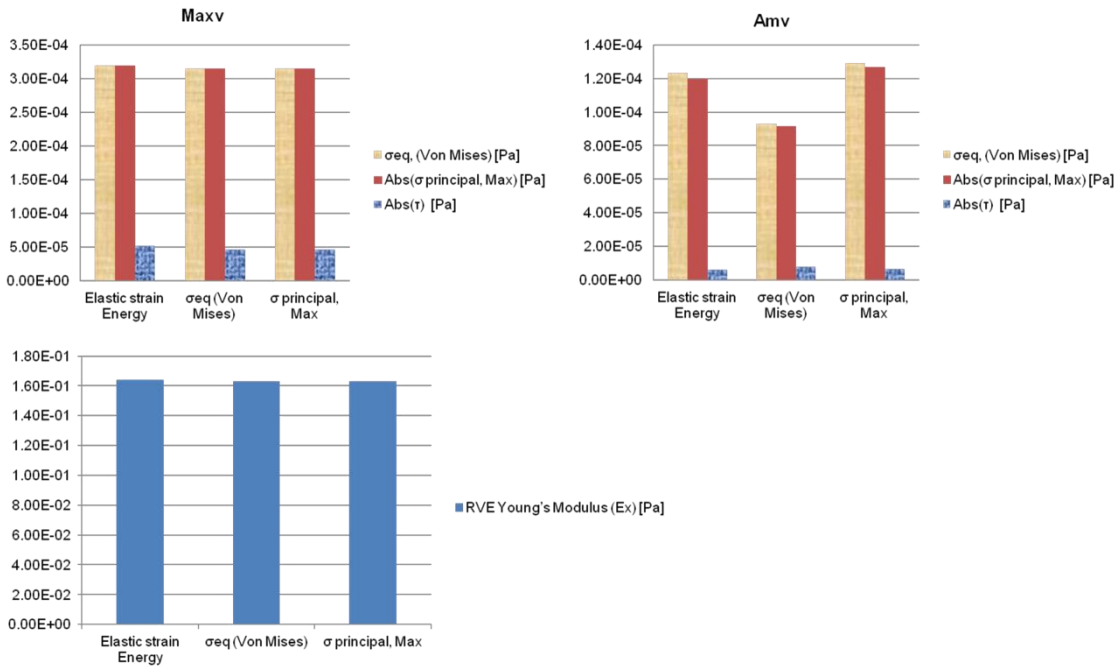

Figure 6. Comparison of the criteria.

As can be seen in Figure 6, regardless of the criterion used, *Maxv* for $\sigma_{eq,\ (von\ Mises)}$ and Abs ($\sigma_{principal,\ Max}$) assume about the same value, while Maxv for Abs (τ) assumes a value of about one order of magnitude lower. The criterion that sorts/eliminates the beams according to σ_{eq} (von Mises) allows to have in output a high homogenized Young's modulus value for the RVE, and, at the same time, to register relatively low *Maxv* for $\sigma_{eq,\ (Von\ Mises)}$ and Abs ($\sigma_{principal,\ Max}$) and moreover a low *Maxv* for Abs (τ). Using this criterion, we also have the lowest *Amv* for the same output results, with the exception of shear stresses that remain over one order of magnitude lower compared to normal stresses. From the structural point of view, in the context of small deformations, the target was the optimization of the structural stiffness. Having to choose an internal configuration of RVE space frame, boundary conditions and amount of material (porosity) being equal, the author chose equivalent von Mises stress criterion for subsequent FEM calculations. This criterion gave a beam configuration that showed a high Young's modulus and recorded inside the less burdensome stress state.

5.2 FEM results

A titanium alloy (Ti-6Al-4V) was chosen for the 3D printing; once printed, this alloy is characterized by the following elastic material properties: E = 119GPa and v = 0.342.

These properties have been introduced as input parameters in the described algorithm for the linear elastic modelling of the beams. In this case PBC have not been applied; in order to take account of the real testing conditions (tensile tests) all the degree of freedom of the nodes belonging to the contact plane between specimen and the titanium bases have been set equal to zero in order to simulate the constraint effect of the titanium base. The calculation of Young's moduli was carried out by applying to the free side of the RVE perpendicular to the tensile axis, an arbitrary displacement and obtaining its reaction force as the sum of the nodal forces. Initial section ($Lrve^2$) has been considered as reference in the calculation. The results of the simulations, in terms of Young's modulus, conducted on the cubic RVEs are collected in Table 4.

Table 4 FEM results.

	RVE
E_x (*MPa*)	659.01
E_y (*MPa*)	16.25
E_z (*MPa*)	8.74

5.3 Experimental results

The results of the uniaxial tensile tests in terms of Young's modulus, conducted on the cubic specimens are collected in Table 5; the reported results are the arithmetic mean value of the five specimens printed for each direction (*X*, *Y* and *Z*) with the corresponding standard deviations.

Table 5 Experimental results.

	RVE
E_x (*MPa*)	677.75 ± 23.65
E_y (*MPa*)	17.55 ± 0.60
E_z (*MPa*)	9.25 ± 0.42

5.4 Comparisons between experimental and FEM results

The histograms reported in Figure 7 shows the comparison of experimental and numerical results in terms of Young's modulus. The percentage relative errors in the calculation of Young's moduli *Ex*, *Ey* and *Ez* are respectively equal to: Er_x=2.77%, Er_y=7.41% and Er_z=5.51%

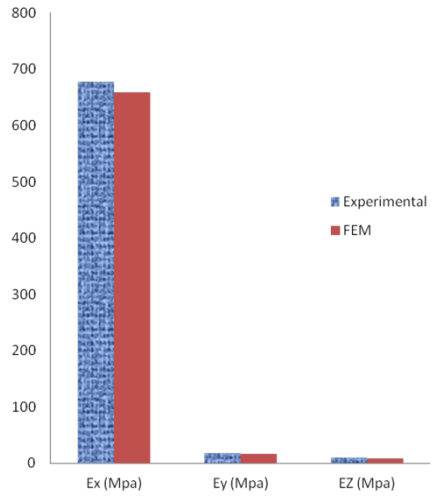

Figure 7. Experimental/numerical correlation in terms of Young's modulus.

6. Discussion, conclusions and perspectives

This work deals with the development, the application and the experimental validation of a procedure based on an original algorithm [14], running in a finite element environment, operating inside a three-dimensional solid of any shape replacing the continuous mass of the solid with an appropriate space-frame structure showing cylindrical beams, sharing with it border and boundary conditions. The algorithm input parameters are: average minimum distance between convergence nodes, target porosity, target ANB, radius of the SSS and beams' mechanical properties. At the beginning, the algorithm generates an appropriate isotropic network of randomly oriented beams; then it adapts the network to the loads induced by the boundary conditions according to an appropriate criterion. At the end, a routine resized the beams according to the target input porosity or to the wanted mechanical stiffness, varying the radius of the circular cross section of the beams.

To show a practical application of the algorithm and for the validation of the final FEM model characterized by a one-dimensional element (beams) based network, a cubic RVE, properly sized, was chosen to simplify the analysis of the mechanical behaviour and material symmetries. By implementing PBC, an *ad hoc* written routine was able to retrieve the whole stiffness matrix of the cubic RVE. In this way, once oriented the beams along a particular direction, the relationship between the compact material Young's modulus in input and the

resulting homogenized Young's modulus of the porous RVE, along the main beam direction (*X*), was estimated.

In this case study, once sized the beams' cross sections according to the desired porosity, the algorithm created a solid model in a CAD system that was converted in .stl file and printed by means of 3D printer using an appropriate titanium alloy. The FEM results in terms of young's moduli were compared with experimental ones obtained by tensile tests conducted on the printed cubic RVEs. The FEM and experimental results were very close with a mean relative error of 5.23% (see figure 7).The worst correspondence between experimental and predicted elastic modulus has been observed along the *X* axis. A three-dimensional element based network usually gives us results more close to reality. In this case, it would have been possible to build a three-dimensional element based FEM model after the realization of the CAD solid model (see section 2.1, step 12). Such a model would have required a very high computational burden significantly impairing the computing speed that is one of the peculiar characteristics of a parametric variational analysis. However in this case, the very good experimental/numerical correlation confirmed the validity of the beam element - based space frame that could be applied to different solid shapes and materials. The algorithm, subjected to further validation, could possibly be applied to other areas of engineering. It can be easily modified in order to be able to control, for example, the average resistant cross section of the beams, or, even better, the resistant cross section of each beam according to the boundary conditions. Possible applications could be the production of those porous materials for which it is required a set value of porosity, a set external shape, a low weight and/or heterogeneity of the mechanical properties at the micro and macro levels as for example in the field of the CATE for production of scaffolds (bone-like structured foams) and in the field of ergonomics for production of highly structured foams. In fact, the introduction of curved beams by introducing specific parametric curves in such a way to have an additional control parameter on the mechanical behaviour of the porous material could be very interesting.

Acknowledgements

We acknowledge the support of the 3F&EDIN S.P.A. (Centro Direzionale E/7 80143 Napoli, Italy) in the 3D printing of the titanium alloy specimens and of Eng. Michele Perrella, Ph.D

(Department of Industrial Engineering, University of Salerno, Via Giovanni Paolo II, 132, 84084 Fisciano, SA, Italy), for the experimental testing phase.

References

[1] Deaton JD, Grandhi RV. A survey of structural and multidisciplinary continuum topology optimization: post 2000. Struct Multidiscip Optim 2014; 49(1): 1–38.

[2] Rozvany GIN. Aims, scope, methods, history and unified terminology of computer-aided topology optimization in structural mechanics. Struct Multidiscipl Optim 2001; 21: 90–108.

[3] Wolff J. The law of bone remodelling. Berlin, Germany: Springer-Verlag, 1986.

[4] Cowin SC. Bone Mechanics Handbook, second ed. USA: CRC Press, 2001.

[5] Fernandes P, Rodrigues H, Jacobs C. A model of bone adaptation using a global optimisation criterion based on the trajectorial theory of Wolff. Comput Methods Biomech Biomed Eng 1999; 2 (2): 125–138.

[6] Garcia JM, Doblaré M, Cegonino J. Bone remodelling simulation: a tool for implant design. Comput Mater Sci 2002; 25: 100–114.

[7] Jacobs CR, Simo JC, Beaupre, GS, Carter, DR. Adaptive bone remodeling incorporating simultaneous density and anisotropy considerations. J Biomech 1997; 30 (6): 603–613.

[8] Cowin SC. Bone stress adaptation models. ASME J Biomech Eng 1993; 115: 528 - 533.

[9] Huiskes R, Hollister SJ. From Structure to process, from organ to cell: recent developments of FE-analysis in orthopaedic biomechanics. ASME J Biomech Eng 1993; 115: 520–527.

[10] Tsubota K, Suzuki Y, Yamada T, Hojo M, Makinouchi A, Adachi T. Computer simulation of trabecular remodelling in human proximal femur using large-scale voxel FE models: approach to understanding Wolff's law. J Biomech 2009; 8: 1088–1094.

[11] Luo ZP, An KN. A theoretical model to predict distribution of the fabric tensor and apparent density in cancellous bone. J Math Biol 1998; 36 (6): 557–568.

[12] Boyle C, Kim IY. Three-dimensional micro-level computational study of Wolff's law via trabecular bone remodelling in the human proximal femur using design space topology optimization. J Biomech 2011; 44 (5): 935–942.

[13] Hambli R, Katerchi H, Benhamou CL. Multiscale methodology for bone remodelling simulation using coupled finite element and neural network computation. Biomech Model Mechanobiol 2011; 10: 133–145.

[14] Naddeo F. 2016 Metodologia per la realizzazione ottimizzata rispetto ai carichi di scaffold tissutali, Patent 102016000047650.

[15] Naddeo F, Baldino L, Cardea S, Naddeo A, Reverchon E. Optimization of an ad hoc realized lattice structure structured RVE for FEM modeling of nanoporous biopolymeric scaffolds obtained by supercritical fluids assisted process. Chem Eng Trans 2016;49: 169-174.

[16] Lakatos É, Bojtár I. Trabecular bone adaptation in a finite element frame model using load dependent fabric tensors. Mech Mater 2012; 44: 130–138.

[17] Ma HS, Pre´vost, JH, Scherer GW. Elasticity of DLCA model gels with loops. Int J Solids Struct 2002; 39: 4605–4614.

[18] Rainer A, Giannitelli SM, Accoto D, Porcellinis S, Guglielmelli E, Trombetta M. Load-Adaptive Scaffold Architecturing: A Bioinspired Approach to the Design of Porous Additively Manufactured Scaffolds with Optimized Mechanical Properties. Ann Biomed Eng 2012; 40(4): 966-75.

[19] Hori M, Nemat-Nasser S. On two micromechanics theories for determining micro - macro relations in heterogeneous solids. Mech Mater 1999; 31: 667–682.

[20] Cricrì G, Garofalo E, Naddeo F, Incarnato L. Stiffness constants prediction of nanocomposites using a periodic 3D-FEM model. J Polym Sci Part B Polym Phys 2012; 50: 207–220.

[21] Naddeo F, Cappetti N, Naddeo A. Automatic versatile parametric procedure for a complete FEM structural analysis of composites having cylinder-shaped reinforcing fibres. Comput Mater Sci 2014; 81: 239–245.

[22] Baldino l, Naddeo F, Cardea S, Naddeo A, Reverchon E. FEM modeling of the reinforcement mechanism of Hydroxyapatite in PLLA scaffolds produced by supercritical drying, for Tissue Engineering applications. J Mech Behav Biomed Mater 2015; 51: 225–236.

[23] Pothuaud L, van Rietbergen B, Charlot C, Ozhinsky E, Majumdar S. A new computational efficient approach for trabecular bone analysis using beam models generated with skeletonized graph technique. Comput Methods Biomech Biomed Eng 2004; 7 (4): 205–213.

[24] van Lenthe GH, Stauber M, Müller R. Specimen-specific beam models for fast and accurate prediction of human trabecular bone mechanical properties. Bone 2006; 39: 1182–1189.

[25] Cappetti N, Naddeo A, Naddeo F, Solitro GF. Finite elements/Taguchi method based procedure for the identification of the geometrical parameters significantly affecting the biomechanical behavior of a lumbar disc. Comput Methods Biomech Biomed Engin 2016; 19(12): 1278-1285.

Figure Captions

Figure 1. Algorithm flow chart showing the fundamental steps used for elaborating a cubic solid mass withstanding generic boundary conditions: A) step 1; B) step 2; C) steps 3 and 4; D) steps 5 - 8 ; E) steps 9 - 13; F) 3D printed metal specimen.

Figure 2. Example of an initial isotropic cubic RVE. For graphical purposes, fewer mesh wires than those used in the calculation are represented.

Figure 3. 3D printed titanium alloy specimen.

Figure 4. Tensile test on the cubic specimen.

Figure 5. Effect of the algorithm elaboration on the cubic RVE: a) isotropic cubic space frame showing the direction of the imposed displacements (*X* axis); b) cubic space frame showing resized beams oriented along the *X* axis; c) 3D printed titanium alloy specimen.

Figure 6. Comparison of the criteria.

Figure 7. Experimental/numerical correlation in terms of Young's modulus.

Tables

Table 1 Morphometric input parameters characterizing the cubic RVE to be printed.

	RVE
Lrve	4cm
dist	Lrve/4
SSS radius	*dist* x 1.75
Porosity	0.96
ANB	6

Table 2 Testing machines characteristics

force capacity:	30kN
load cell accuracy:	class 0.5
position resolution:	0.001 mm
position accuracy:	0.01 mm
axial extensometers	MTS 634.12F-24
gage lenght	25 mm
accuracy class	0.5 mm

Table 3 Cubic RVE stiffness matrix: the values were rounded to the first decimal place to better show the tendency to a transversely isotropic behaviour.

$K_{11} = 24.7$	$K_{12} = 1.7$	$K_{13} = 1.8$	$K_{14} = 0.0$	$K_{15} = 0.0$	$K_{16} = 0.0$
$K_{21} = 1.7$	$K_{22} = 0.6$	$K_{23} = 0.1$	$K_{24} = 0.0$	$K_{25} = 0.0$	$K_{26} = 0.0$
$K_{31} = 1.8$	$K_{32} = 0.1$	$K_{33} = 0.6$	$K_{34} = 0.0$	$K_{35} = 0.0$	$K_{36} = 0.0$
$K_{41} = 0.0$	$K_{42} = 0.0$	$K_{43} = 0.0$	$K_{44} = 0.1$	$K_{45} = 0.0$	$K_{46} = 0.0$
$K_{51} = 0.0$	$K_{52} = 0.0$	$K_{53} = 0.0$	$K_{54} = 0.0$	$K_{55} = 1.9$	$K_{56} = 0.0$
$K_{61} = 0.0$	$K_{62} = 0.0$	$K_{63} = 0.0$	$K_{64} = 0.0$	$K_{65} = 0.0$	$K_{66} = 2.0$

Table 4 FEM results.

	RVE
E_x (*MPa*)	659.01
E_y (*MPa*)	16.25
E_z (*MPa*)	8.74

Table 5 Experimental results.

	RVE
E_x (*MPa*)	677.75 ± 23.65
E_y (*MPa*)	17.55 ± 0.60
E_z (*MPa*)	9.25 ± 0.42

Table

Tables

Table 1 Morphometric input parameters characterizing the cubic RVE to be printed.

	RVE
Lrve	4cm
dist	Lrve/4
SSS radius	*dist* x 1.75
Porosity	0.96
ANB	6

Table 2 Testing machines characteristics

force capacity:	30kN
load cell accuracy:	class 0.5
position resolution:	0.001 mm
position accuracy:	0.01 mm
axial extensometers	MTS 634.12F-24
gage lenght	25 mm
accuracy class	0.5 mm

Table 3 Cubic RVE stiffness matrix: the values were rounded to the first decimal place to better show the tendency to a transversely isotropic behaviour.

K_{11} = 24.7	K_{12} = 1.7	K_{13} = 1.8	K_{14} = 0.0	K_{15} = 0.0	K_{16} = 0.0
K_{21} = 1.7	K_{22} = 0.6	K_{23} = 0.1	K_{24} = 0.0	K_{25} = 0.0	K_{26} = 0.0
K_{31} = 1.8	K_{32} = 0.1	K_{33} = 0.6	K_{34} = 0.0	K_{35} = 0.0	K_{36} = 0.0
K_{41} = 0.0	K_{42} = 0.0	K_{43} = 0.0	K_{44} = 0.1	K_{45} = 0.0	K_{46} = 0.0
K_{51} = 0.0	K_{52} = 0.0	K_{53} = 0.0	K_{54} = 0.0	K_{55} = 1.9	K_{56} = 0.0
K_{61} = 0.0	K_{62} = 0.0	K_{63} = 0.0	K_{64} = 0.0	K_{65} = 0.0	K_{66} = 2.0

Table 4 FEM results.

	RVE
E_x (*MPa*)	659.01
E_y (*MPa*)	16.25
E_z (*MPa*)	8.74

Table 5 Experimental results.

	RVE
E_x (*MPa*)	677.75 ± 23.65
E_y (*MPa*)	17.55 ± 0.60
E_z (*MPa*)	9.25 ± 0.42

Figure 1
Click here to download high resolution image

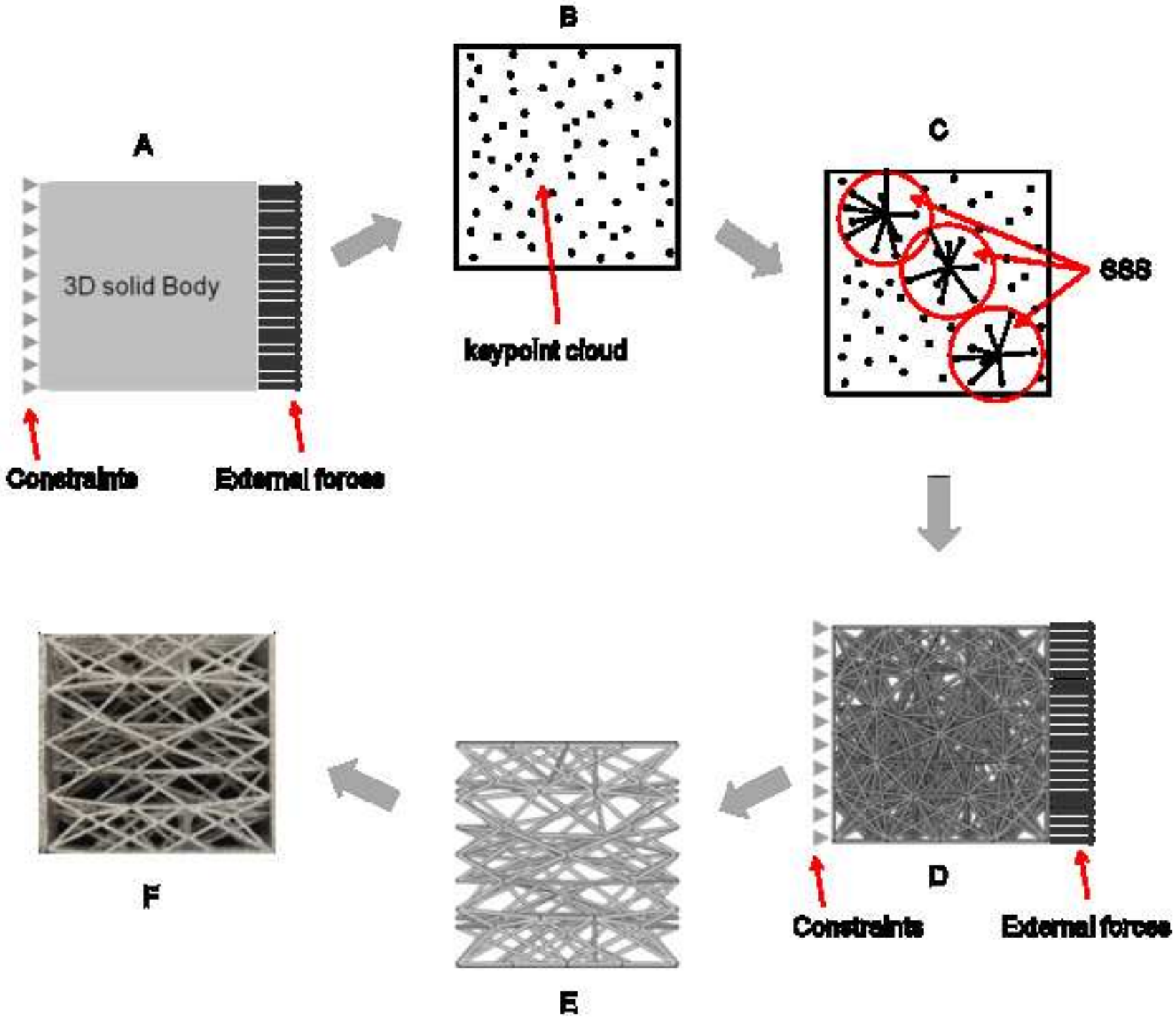

Figure 2

Click here to download high resolution image

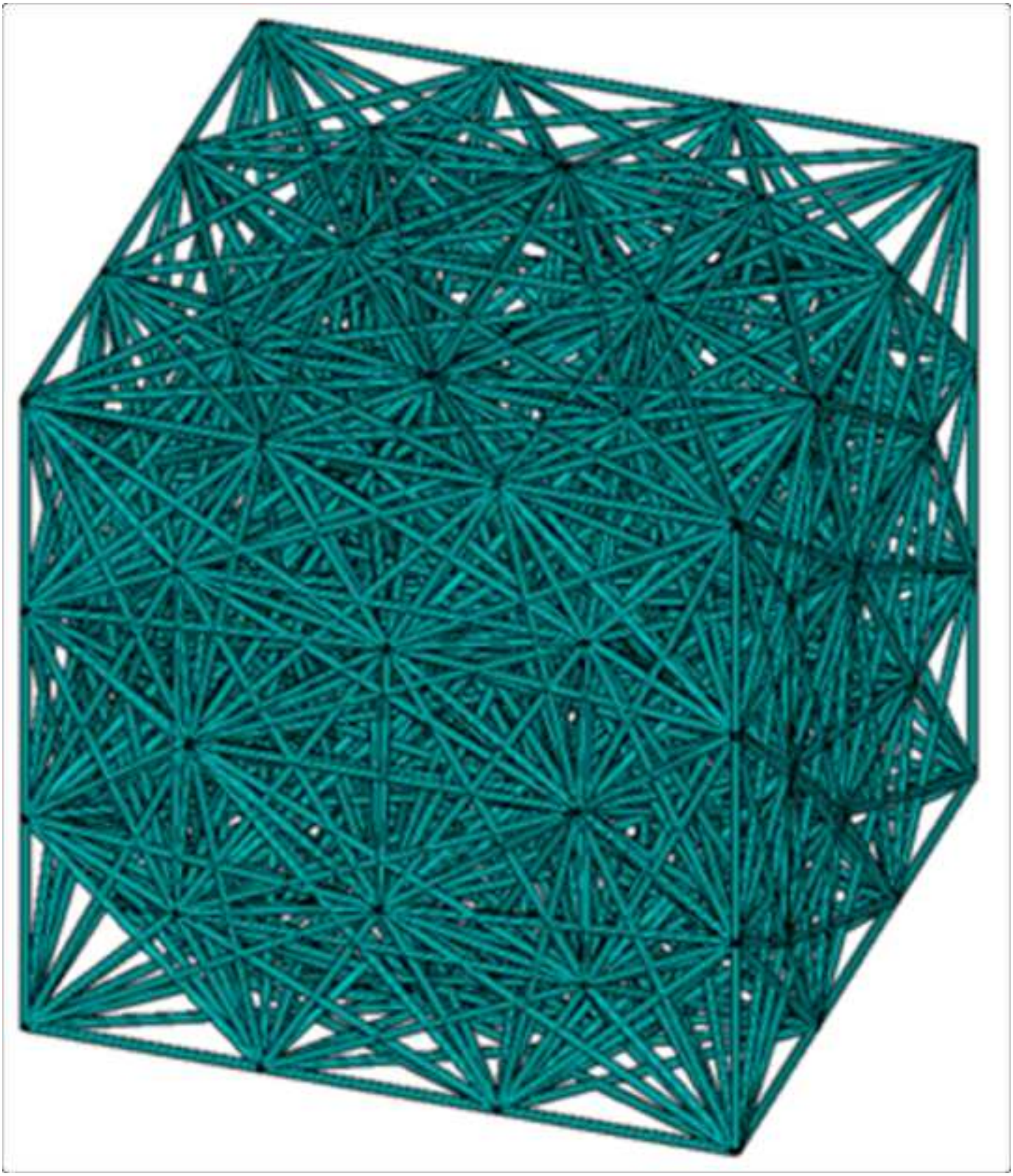

Figure 3

Click here to download high resolution image

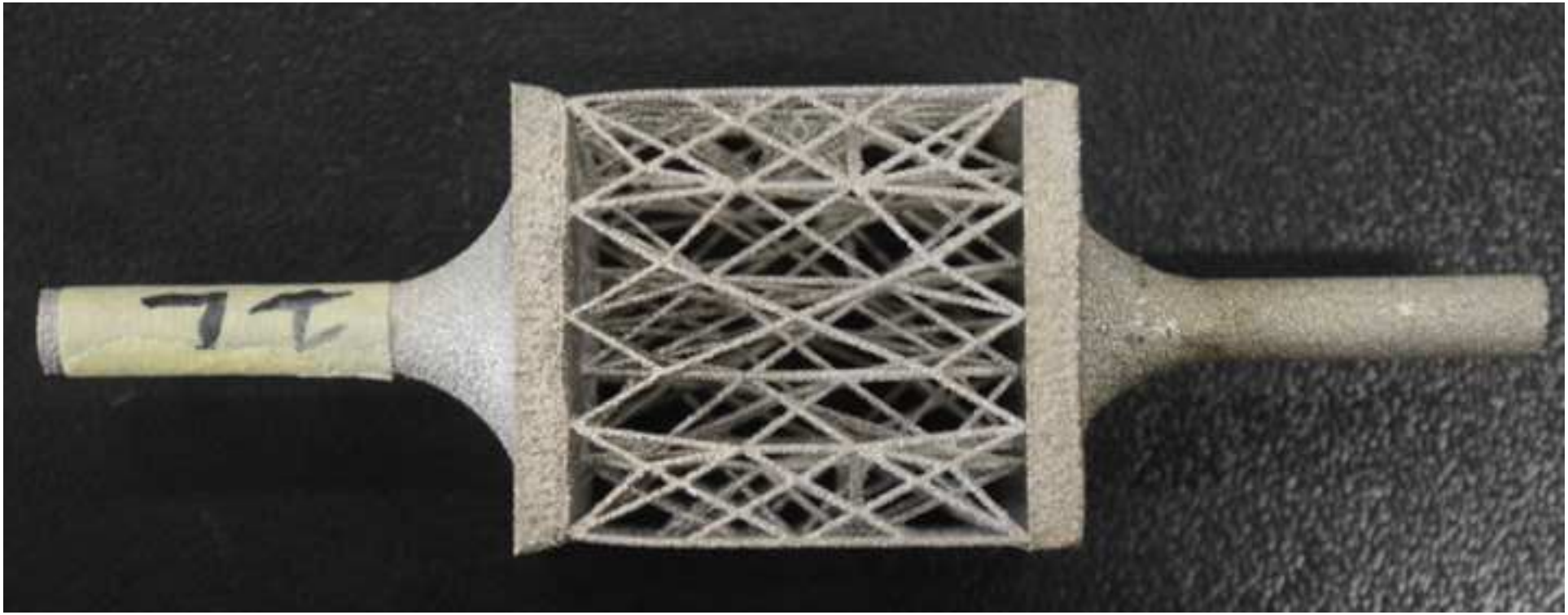

Figure 4

Click here to download high resolution image

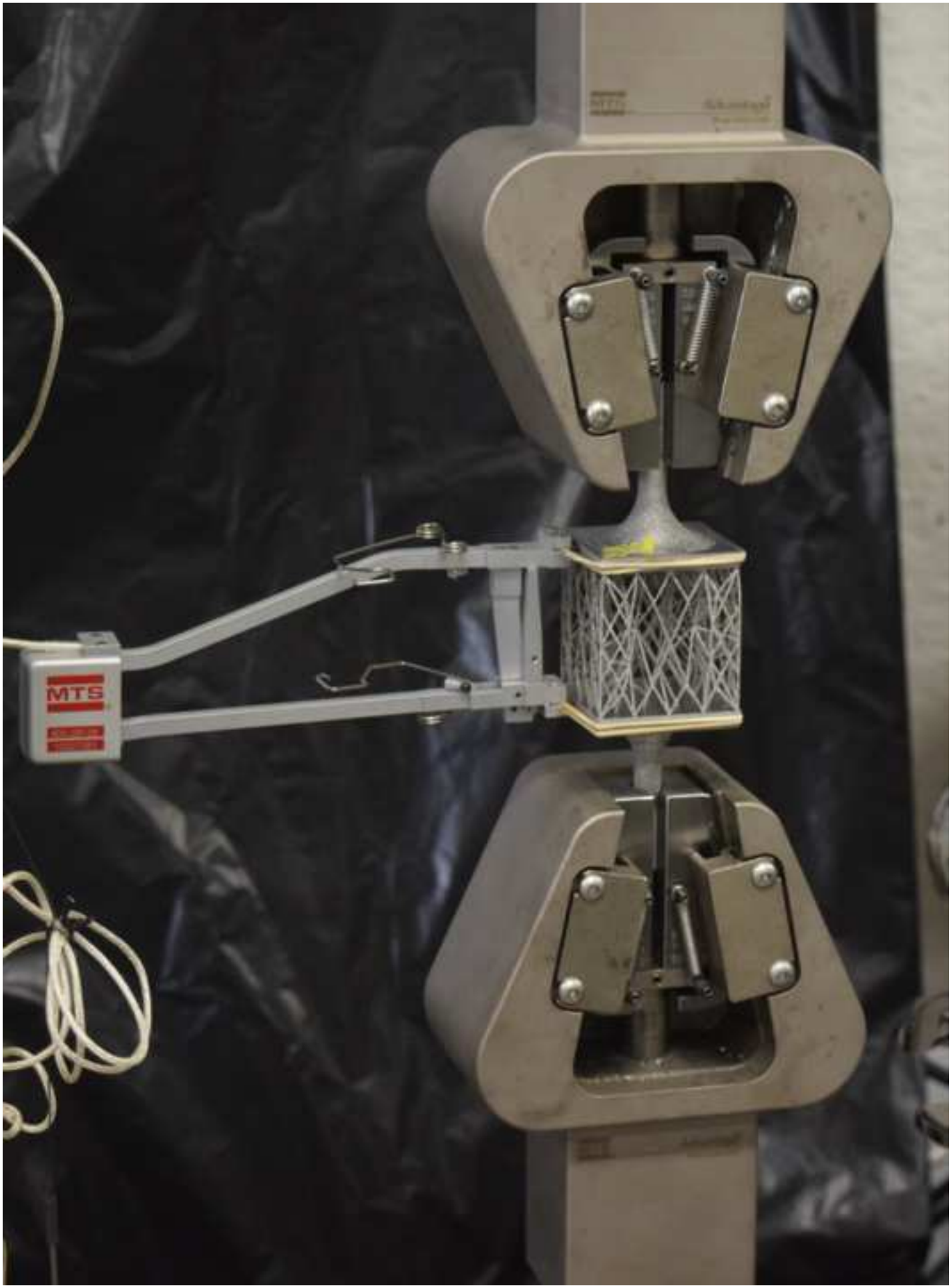

Figure 5

Click here to download high resolution image

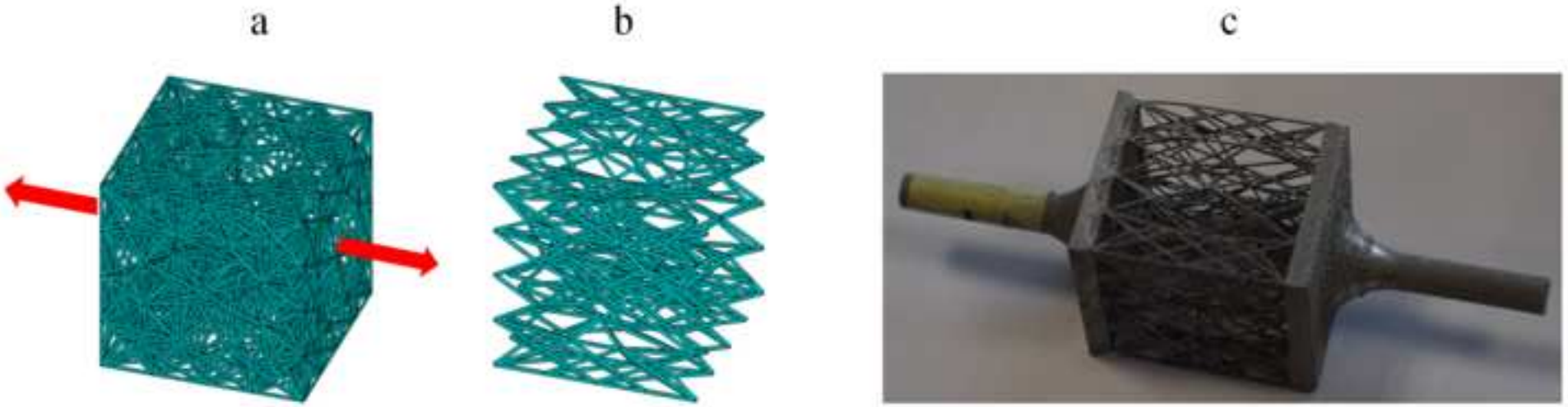

Figure 6

Click here to download high resolution image

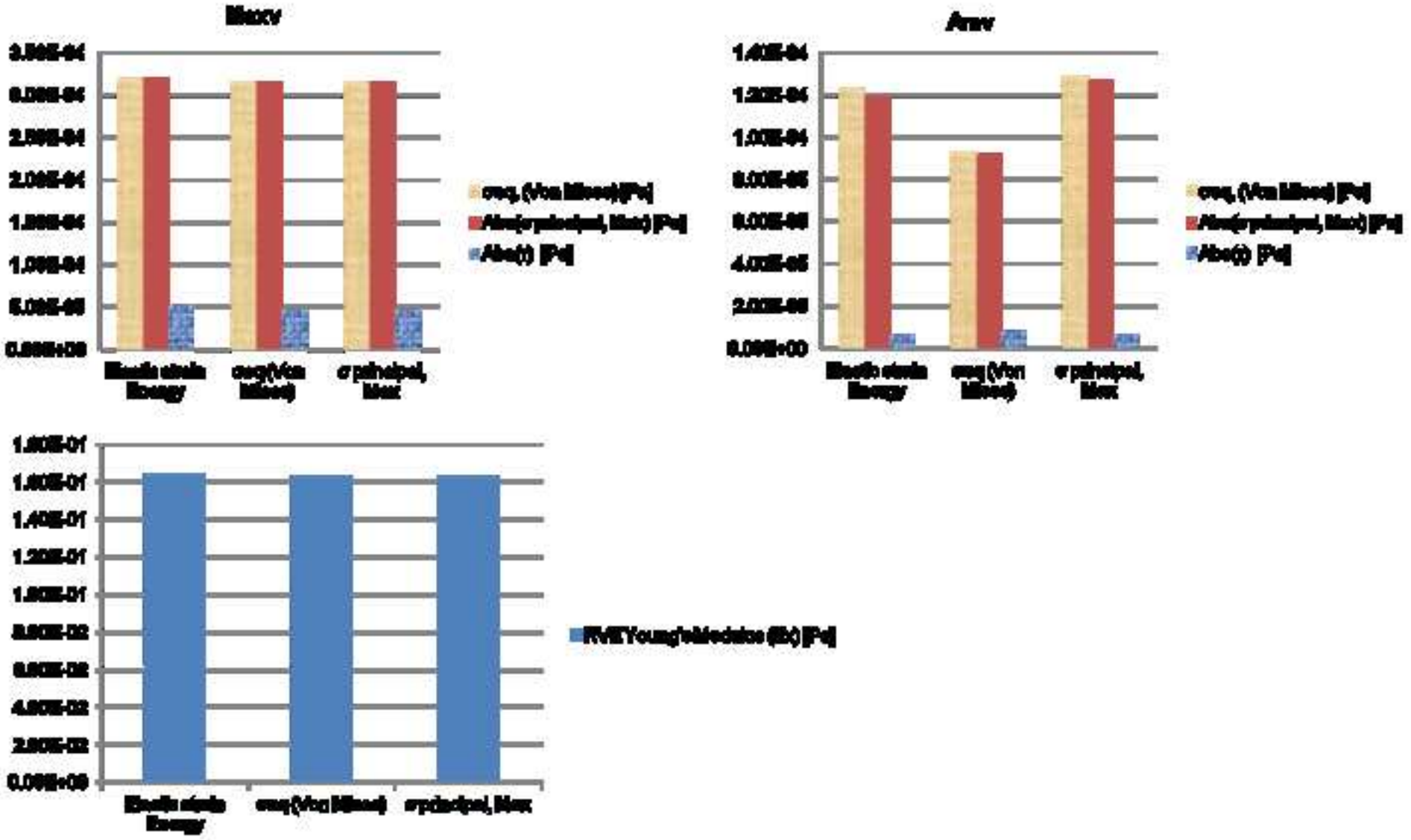

Figure 7

Click here to download high resolution image